50th AIAA Aerospace Sciences Meeting including the New Horizons Forum and Aerospace Exposition
09 - 12 January 2012, Nashville, Tennessee
AIAA 2012-1086

Finite roughness effect on modal growth of a hypersonic boundary layer

Kahei Danny Fong[1], Xiaowen Wang[2], and Xiaolin Zhong[3]
University of California, Los Angeles, CA, 90095, USA

Numerical simulation of roughness effect on modal growth is conducted on a hypersonic flat-plate at Mach 5.92. The steady base flow is firstly simulated by solving compressible Navier-Stokes equations. Stability characteristics of boundary-layer waves are analyzed by linear stability theory (LST). In stability simulations, two-dimensional disturbances corresponding to mode S or mode F at a frequency of 100 kHz are introduced near the leading edge of the flat-plate. Roughness with adjustable height is placed into four locations with respect to the disturbance synchronization point. It is found that upstream of synchronization point, disturbance is amplified by roughness with a stronger strength for taller roughness. On the other hand, disturbance is damped when the roughness is placed at or downstream of synchronization point. Different from upstream cases, tall roughness damps disturbance instead of amplifying it. We believe the relative location of synchronization point and roughness is a candidate to explain roughness delay transition as previous experiments have shown. Our results also show that roughness effect on mode S and mode F are very alike. In addition, a disturbance with a wide bandwidth is planned and will be imposed in the future.

I. Introduction

The physical mechanisms of the roughness induced boundary-layer transition is critical to the development of hypersonic vehicles [1]. Transition can have a first-order impact on the lift and drag, stability and control, and heat transfer properties of the vehicles [2]. For example, roughness induced transition is an important consideration in the design of thermal protection systems (TPS) of hypersonic vehicles [3, 4]. For a reentry vehicle entering earth's atmosphere, it initially experiences a heating environment associated with a laminar boundary layer. As the vehicle altitude decreases, the vehicle surface becomes rougher and the boundary layer becomes turbulent. The transition from a laminar boundary layer to a turbulent one leads to the increase of surface heating rates by a factor of five or more. Thus the ability to understand and predict the physics of roughness induced transition plays an essential role in the design of TPS for reentry vehicles. Currently, roughness induced laminar-turbulent transition in hypersonic boundary layers, especially that induced by arbitrary surface roughness, is still poorly understood due to the limitation in experimental facilities and numerical methods [5].

Ideally the laminar-turbulent transition process can be divided into four stages. The first involves small disturbance fields which are initialized via a process termed "receptivity" by the viscous flow. The initial disturbance fields can involve both freestream and vehicle self-induced fluctuations such as acoustics, dynamic vortices, entropy spottiness, etc. The next stage is the linear growth stage, where small disturbances are amplified until they reach certain amplitude where nonlinear effects become important. The amplification can be in the form of exponential growth of eigenmodes (Tollmien-Schlichting waves or Mack waves) and nonmodal growth of optimal disturbances (Transient growth). Once a disturbance has reached a finite amplitude, it often saturates and transforms the flow into a new, possibly unsteady state, which is termed as the secondary instability stage. The last stage is the breakdown stage where nonlinearities and/or high-order instabilities excite an increasing number of scales and frequencies in the flow.

The receptivity study is mainly concerned with the excitation of instability waves, the characteristics of which can be analyzed by the linear stability theory (LST) [6]. The LST analyzes the propagation of individual sinusoidal waves in the streamwise direction inside the boundary layer. These waves are referred as Tollmien-Schlichting (T-S) waves for low speed flow, whose amplitudes vary though the boundary layer and die off exponentially outside the boundary layer. Extensive numerical and theoretical researches have been conducted to solve the linearized Navier-

[1] Graduate Research Assistant, Mechanical and Aerospace Engineering Department.
[2] Research Associate, Mechanical and Aerospace Engineering Department, AIAA Senior Member.
[3] Professor, Mechanical and Aerospace Engineering Department, AIAA associate fellow.

Stokes equations and many characteristics regarding the instability waves in hypersonic boundary layers have been discovered [6-10]. Mack [6] identified the unstable modes by using the LST for compressible flow. He showed that inside a supersonic boundary layer, there are multiple higher instability modes in addition to the first mode, which is the compressible counterpart of T-S waves in the incompressible boundary layers. These instability modes in the supersonic boundary layer are termed as first mode, second mode, third mode, etc. For supersonic boundary layer with Mach number larger than four, Mack's second mode is the most unstable mode, and it plays an important role in hypersonic boundary layer transition.

Direct numerical simulation has become an effective research tool for studying hypersonic boundary layer receptivity, stability, and transition by numerically solving the time-dependent three-dimensional Navier–Stokes equations for the temporally or spatially evolving instability waves. Malik et al. [11] investigated the responses of a Mach 8 flow over a sharp wedge of a half-angle of 5.3^o to three types of external forcing: a planar freestream acoustic wave, a narrow acoustic beam enforced on the bow shock near the leading edge, and a blowing-suction slot on the wedge surface. They concluded that these three types of forcing eventually resulted in the same type of instability waves in the boundary layer. Ma and Zhong [12] studied the receptivity mechanisms of the same hypersonic boundary layer to various freestream disturbances, i.e., fast and slow acoustic waves, vorticity waves, and entropy waves, by solving the two-dimensional compressible Navier-Stokes equations. They found that the stable modes in the boundary layer played a very important role in the receptivity process. Recently, Wang et al. [13] further studied the response of the Mach 8 flow over a 5.3^o half-angle sharp wedge to wall blowing–suction. The results showed that mode S is strongly excited when the actuator is located upstream of the corresponding synchronization point. There is no significant amplification of pressure perturbation when the actuator is downstream of the synchronization point. Although the exact cause and mechanism of this result were not clear, such a result was obtained for wall blowing–suction at all frequencies considered in their study. Balakumar [14] numerically investigated the receptivity of a 2-D roughness to acoustic waves and found the isolated roughness does not contribute much in generating unstable disturbances. Marxen et al. [15] simulated the effects of a localized two-dimensional roughness element on the disturbance amplification in a hypersonic boundary layer. Their numerical experiments showed that in the vicinity of the separation regions, which are located in the upstream and downstream of the roughness, an increased amplification of a second-mode disturbance occurs for a certain frequency.

Previous studies showed that the roughness location plays an important role in the developments of mode S excited by the blowing-suction slot [16]. In this paper, we further investigate the finite roughness effect on modal growth of a Mach 5.92 flat-plate boundary layer, mainly focusing on roughness height and roughness location. The steady base flow is firstly simulated by solving compressible Navier-Stokes equations. Stability characteristics of boundary-layer waves are analyzed by linear stability theory (LST). In stability simulations, two-dimensional disturbances corresponding to mode S (slow acoustic wave) or mode F (fast acoustic wave) at a frequency of 100 kHz are introduced near the leading edge. Two dimensional finite roughness with adjustable height is put downstream of the disturbances, as shown in Figure 1. Our results show that roughness height has a significant impact on the spatial development of mode S and F. Roughness amplifies disturbance in the upstream region with the amplification rate depending on roughness height. Downstream of the roughness, the amplified disturbance is damped. Overall, the disturbance is amplified if roughness is placed upstream of synchronization point. In contract, if roughness is placed downstream of synchronization point, disturbance is damped. The damping effect gets more pronounced with taller roughness element.

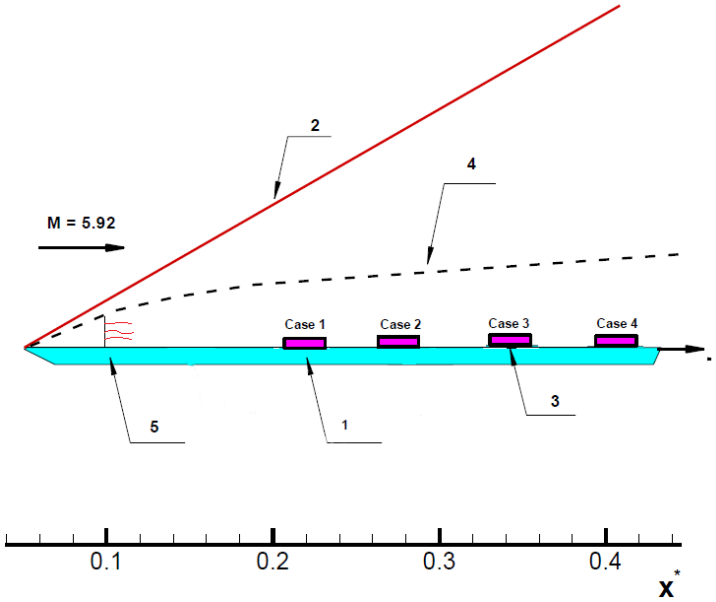

Figure 1. A schematic of the problem: 1. Roughness 2. Bow Shock 3. Synchronization point 4. Boundary layer 5. Pure Mode S or Mode F based on LST results

II. Governing Equations

For direct numerical simulation of hypersonic boundary layer transition, the governing equations are the three-dimensional Navier–Stokes equations. We assume that we are dealing with Newtonian fluids with the perfect gas assumption and isothermal or adiabatic wall conditions. The governing equations can be written in the following conservation-law form in the Cartesian coordinates,

$$\frac{\partial U}{\partial t}+\frac{\partial F_j}{\partial x_j}+\frac{\partial F_{vj}}{\partial x_j}=0 \tag{1}$$

where U , F_j and F_{vj} are the vectors of flow variables, convective flux, and viscous flux in the *jth* spatial direction respectively, i.e.,

$$U=\{\rho,\rho u_1,\rho u_2,\rho u_3,e\} \tag{2}$$

$$F_j=\begin{Bmatrix}\rho u_j\\ \rho u_1u_j+p\delta_{1j}\\ \rho u_2u_j+p\delta_{1j}\\ \rho u_3u_j+p\delta_{1j}\\ (e+p)u_j\end{Bmatrix} \tag{3}$$

$$F_{vj} = \begin{Bmatrix} 0 \\ \tau_{1j} \\ \tau_{2j} \\ \tau_{3j} \\ \tau_{jk}u_k - q_j \end{Bmatrix} \tag{4}$$

In this paper, only perfect-gas hypersonic flow is considered, i.e.,

$$p = \rho RT \tag{5}$$

$$e = \rho(C_v T + \frac{1}{2}u_k u_k) \tag{6}$$

$$\tau_{ij} = \mu(\frac{\partial u_i}{\partial x_j} + \frac{\partial u_j}{\partial x_i}) + \delta_{ij}\lambda\frac{\partial u_k}{\partial x_k} \tag{7}$$

$$q_j = -k\frac{\partial T}{\partial x_j} \tag{8}$$

where R is the gas constant. The specific heat C_v is assumed to be constant with a given ratio of specific heats γ. The viscosity coefficient μ can be calculated by Sutherland's law in the form:

$$\mu = \mu_r \left(\frac{T}{T_0}\right)^{3/2} \frac{T_0 + T_s}{T + T_s} \tag{9}$$

where, for air, $\mu_r = 1.7894\times10^{-5} Ns/m^2, T_0 = 288.0K, T_s = 110.33K$ and λ is assumed to be $-2/3\mu$. The heat conductivity coefficient k can be computed through a constant Prantl number.

III. Numerical Method – High-Order Cut-Cell Method

A schematic of a computational domain and a cut-cell grid in roughness induced hypersonic boundary layer transition is shown in Figure 2. This figure shows a typical hypersonic flow over a blunt body, where a bow shock is created by the supersonic freestream. In this paper, a high-order shock-fitting method is used to track the movement of the bow shock which is treated as the upper boundary of the computational domain. The computational grid for a shock-fitting formulation is bounded between the bow shock above and the blunt body below. The cut-cell grid is a smooth curvilinear grid fitted to the baseline body shape without the roughness. As a result, the roughness surface cuts across the grid lines. The roughness surface, Γ, is represented by surface equation in the following form,

$$\Gamma: f(x, y, z) = 0 \tag{10}$$

For a problem concerning practical arbitrary roughness, it is likely that there is no analytical equation applicable to represent the shape of the roughness element. In this case, a set of n discrete points $\{(x_1, y_1, z_1), (x_2, y_2, z_2), ..., (x_n, y_n, z_n)\}$ are used to represent the surface.

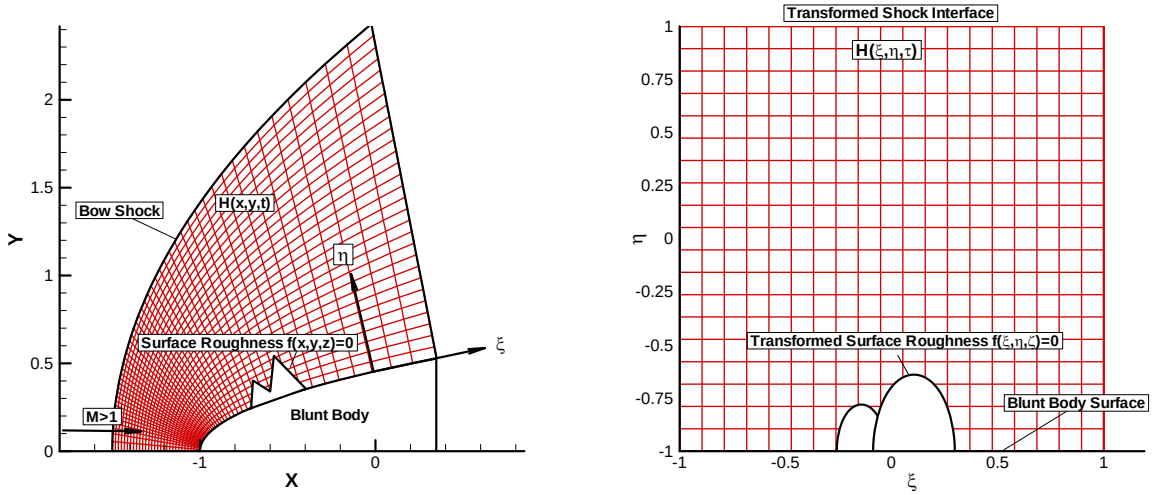

(a) **(b)**

Figure 2.Physical and computational domain and a cut-cell grid of hypersonic flow over a blunt body with surface roughness: a) physical grid, b) computational grid with a transformed roughness

Both the governing Eq. (1) and the roughness equation (10) in the physical domain are transformed into a Cartesian computational domain bounded by bow shock and flat plate. Under the computational coordinate system, the body fitted grids are represented by a curvilinear three-dimensional coordinates (ξ,η,ς) along the grid lines. The unsteady movement of the bow shock is treated as the computational upper boundary located at $\eta=\eta_{\max}$, which is time dependent. The other grid lines $\xi=const$ and $\varsigma=const$ remains stationary during computations. The coordinate transformation is defined by:

$$\begin{cases}\xi=\xi(x,y,z)\\ \eta=\eta(x,y,z,t)\\ \varsigma=\varsigma(x,y,z)\\ \tau=t\end{cases}\leftrightarrow\begin{cases}x=x(\xi,\eta,\varsigma,\tau)\\ y=y(\xi,\eta,\varsigma,\tau)\\ z=z(\xi,\eta,\varsigma,\tau)\\ t=\tau\end{cases}\tag{11}$$

where (x,y,z,t) are the physical coordinates defined under Cartesian coordinate system.

A third-order accurate Cut-Cell method is used in current numerical simulation [17]. A set of uniformly distributed Cartesian grids can be generated in the computational domain where the grid distribution in the physical domain is not uniformly distributed. Because smooth body-fitted grids are generated in the regular computational domain without the roughness, some of the Cartesian grid cells may be cut by the roughness boundary, which leads to irregular Cartesian grid cells. More details of the grid structure are discussed in a previous paper [17].

IV. Results and Discussions

A. Flow conditions and roughness model

In this paper, the new cut-cell method is used to compute hypersonic viscous flow over a flat plate with an isolated surface roughness element (Figure 2). Both steady and unsteady flows are considered. The freestream flow conditions are the same as those used in Maslov's experiment [7] as follows,

$$\begin{cases} P_r = 0.72, R_\infty = \rho_\infty * u_\infty / \mu_\infty = 13.2\times 10^6 / m \\ M_\infty = 5.92, T_\infty = 48.69K, P_\infty = 742.76Pa \end{cases} \tag{12}$$

where M_∞, T_∞, P_∞, P_r, R_∞ are Mach number, temperature, pressure, Prandtl number and unit Reynolds number, respectively. The flat plate is assumed to be isothermal. The total length of the flat plate is about 1.69m.

In this section, unless stated otherwise, most flow variables are presented as dimensionless ones. The main exception is that the x and y coordinates are presented in dimensional form so that the simulation results can be easily related to the experimental setup. For other variables, we nondimensionalize the flow velocities by the freestream velocity u_∞, density by ρ_∞, pressure by $\rho_\infty (u_\infty)^2$, and temperature by T_∞.

An isolated roughness element of smooth shape is placed on the surface of the flat plate. Motivated by Whiteheard's experiments [18], the shape of the surface roughness is chosen to be a two-dimensional bump, governed by the following elliptic equation,

$$\frac{(x-x_c)^2}{a^2} + \frac{y^2}{b^2} = h^2 \tag{13}$$

where the parameters a, b and h control roughness width and height. In our test cases, roughness width is fixed at 4 times local boundary layer thickness while the height ranges from 25% to 62.5% of local boundary layer thickness. In addition, x_c defines the location of the roughness center. The grid size is 241 points in streamwise direction and 121 points in wall-normal direction in each computational zone.

A third-order cut-cell method described in Section III is used to compute the two-dimensional viscous hypersonic flow over the flat plate with the roughness element. As described in Section III, a coordinate transformation is employed to transform the physical domain shown in Figure 3 into a rectangle computational domain with a set of Cartesian grid. The optimal transformation formula is determined by the specific physical problem considered. For viscous flow over a flat plate, it is necessary to cluster more grid points near wall surface in order to resolve the viscous boundary layer.

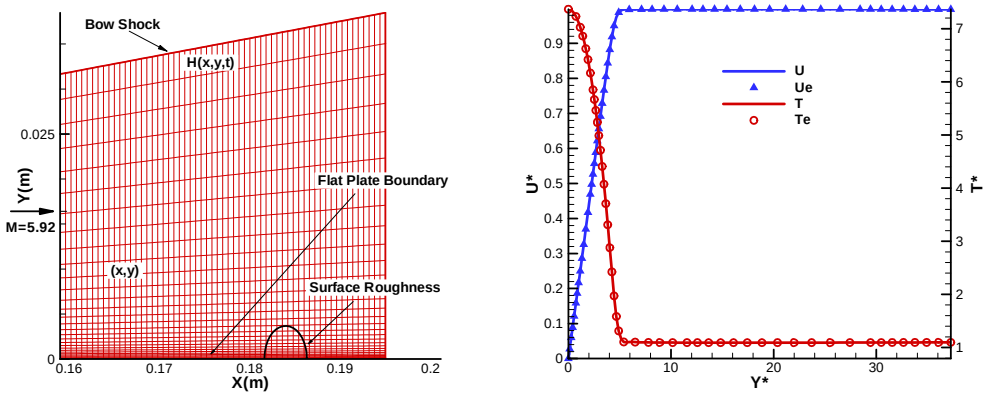

Figure 3. (a) Computational grid for hypersonic flow over a flat plate with an isolated surface roughness (showing one out of four grid points in both directions), (b) Comparison of the current shock-fitting results with theoretical solutions for temperature and wall-normal velocity distributions across the boundary layer at $x = 0.1676m$ [16].

In the first step of the transformation, the entire physical domain shown in Figure 3 is transformed into a square domain defined on $[0,1]\times[0,1]$ as an intermediate coordinate space. The transformation relation is defined as:

$$\begin{cases} X = \dfrac{x - x_{strart}}{L} \\ Y = \dfrac{y}{H(x,y)} \end{cases} \tag{14}$$

where (X,Y) is defined under the intermediate coordinate system, L is the streamwise length of the flat plate in physical domain, x_{start} is the streamwise coordinate of starting point of computation domain, and the distance along η direction between the solid wall and bow shock is referred to H.

In the second step of the transformation, the intermediate coordinate in the (X,Y) space is mapped into the final computational domain (ξ,η) in order to cluster more grid points into the viscous boundary layer near the flat plate surface. In the present study, an exponential stretch function is used to cluster grids in the η direction as follows,

$$\begin{cases} X = \xi \\ Y = -\dfrac{\left(\dfrac{\beta+1}{\beta-1}\right)^{(1-\eta)} - 1}{\left(\dfrac{\beta+1}{\beta-1}\right)^{(1-\eta)} + 1}\beta \end{cases} \tag{15}$$

where β is the stretching parameter. The value of $\beta = 1.01$ is used in the current simulation. With this β value, about 50% of the total grid points in the η direction are clustered inside the boundary layer. The combination of the transformations of these two steps leads to overall transformation by Eq. (11).

In the computational domain $(\xi,\ \eta)$, the baseline grid is a set of Cartesian grid similar to the schematic shown in Figure 2(b). The intersection of the roughness surface with the grid lines creates cut cells, which are treated by the current cut-cell method. The surface Equation (13) of the roughness surface is transformed into the computational domain in order to apply the cut-cell method. By substituting Eqs. (14) and (15) into the roughness surface Eq. (13), the analytical equation for roughness surface in the computational domain can be written as

$$f(\xi,\eta) = \frac{(L\xi)^2}{a^2} + \frac{\ell H(\xi L + x_{start})^2}{b^2} - h^2 = 0$$
$$\text{where } \ell = \frac{\left(\dfrac{\beta+1}{\beta-1}\right)^{(1-\eta)} - 1}{\left(\dfrac{\beta+1}{\beta-1}\right)^{(1-\eta)} + 1}\beta \tag{16}$$

From Eq. (16), we can calculate the coordinates of the boundary points by computing the coordinates of the intersection between the roughness surface and the grid lines. For a given value of ξ along the roughness surface, the Newton iteration method is employed to solve Eq. (16) for the corresponding value of η for a boundary point, and vice versa. Having computed the boundary points, we can identify all irregular and dropped points near the roughness surface. The remaining grid points are regular points. After computing all coordinates of the irregular, regular, boundary and dropped points, the high-order cut-cell method is applied to solve governing equations.

B. Steady flow solution without surface roughness

The steady mean flow solutions are calculated by using the fifth-order shock-fitting method. But in the leading edge region of the flat plate, there is a singularity at the tip of the plate and the high-order shock fitting method cannot be used there. Thus a second-order total variation diminishing (TVD) shock-capturing method, which follows that used by Lee et al. [19], is employed to calculate a small local flow field around the tip of the flat plate. The computational domain for the TVD calculations starts at $x = -0.006m$ and ends at a very short distance downstream of the leading edge at $x = 0.003m$. Having obtained the steady solutions near the leading edge, we then use the solution of the TVD scheme as the inlet condition to start the subsequent shock-fitting calculations. The computational domain for the high-order shock-fitting methods starts at $x = 0.003m$ and ends at $x = 1.68784m$. In actual simulations, the computational domain is divided into 30 zones, with total of 5936 grid points in the streamwise direction and 121 points in the wall-normal direction. As mentioned above, the second zone uses the results of the first zone of the second-order TVD solution as the inlet condition. A later zone uses the interpolation of its former zone's data as the inlet condition.

The solutions for the steady viscous flow over the flat plate with no surface roughness are first obtained. Figure 3 shows the streamwise velocity and temperature profiles along the wall-normal direction at $x = 0.1676m$. The current numerical solutions obtained by the fifth-order shock-fitting scheme are compared with the self-similar boundary layer solution. In order to compare with the self-similar solution, the y coordinate is nondimensionalized by $\sqrt{x\mu_\infty / \rho_\infty u_\infty}$. Figure 3(b) illustrates that the results of the current numerical simulation agree very well with the theoretical solutions near the wall. The second-order TVD scheme is accurate enough to be used as the inlet condition of the fifth-order shock-fitting method downstream of the leading edge.

C. Stability characteristics of boundary-layer waves

Stability characteristics of boundary-layer waves of the Mach 5.92 flow is studied by LST using a multi-domain spectral method of Malik [20]. The dimensionless frequency used for linear stability analysis is defined as

$$F = \frac{2\pi f \nu}{u_\infty^2} \tag{17}$$

where F is dimensionless frequency, ν is kinematic viscous coefficient. In present simulation, $\nu = 6.05 \times 10^{-5} m^2 / s$, $F = 5.30 \times 10^{-5}$ for the case of $f = 100kHz$ and $u_\infty = 827.29m / s$.

In LST analyses of boundary layer flows, the Reynolds number based on the local length scale of boundary layer thickness δ. They are expressed as

$$R = \frac{\rho_\infty u_\infty \delta}{\mu_\infty}, \delta = \sqrt{\frac{\mu_\infty x}{\rho_\infty u_\infty}} \tag{18}$$

Hence the relation between R and the unit Reynolds number R_∞ is,

$$R = \sqrt{R_\infty x} \tag{19}$$

with the definitions of Reynolds number R and the dimensionless frequency F, the dimensionless circular frequency ω can also be expressed as

$$\omega = RF \tag{20}$$

Figure 4 shows the eigenvalue spectra of boundary-layer waves at a frequency of 100 kHz at x = 0.189 m. The figure shows wave spectra corresponding to fast acoustic wave, entropy and vorticity waves, and slow acoustic wave. The two discrete waves marked by circles are modes F and S, respectively. Mode F originates from fast acoustic

spectrum on the left side of the figure and passes entropy and vorticity spectra at the center as dimensionless frequency increases. Mode S originates from slow acoustic spectrum on the right side of the figure. It becomes unstable in certain range of dimensionless frequency. The figure also shows that mode S at this frequency is unstable at x = 0.189 m with $\alpha_i < 0$.

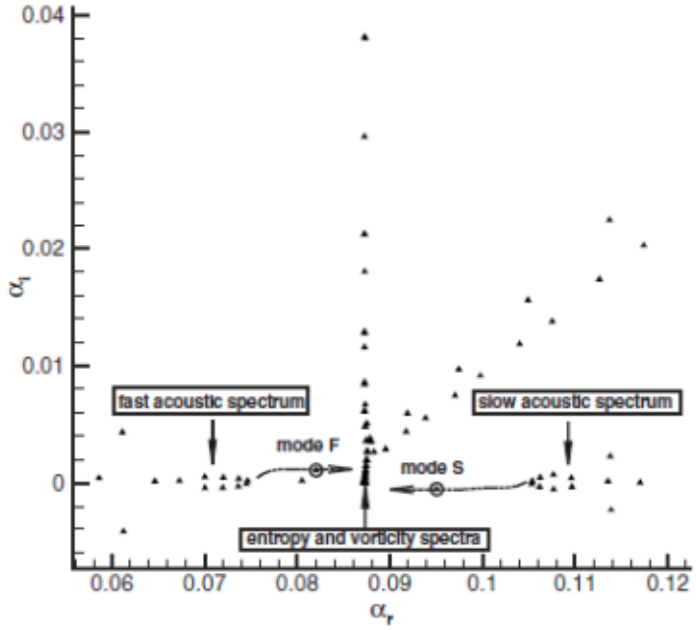

Figure 4. Eigenvalue spectra of boundary-layer waves at the frequency of f=100 kHz at x=0.189 m.

Figure 5 shows phase velocities of boundary-layer waves at two locations of x=0.159 m and x=0.189 m as a function of circular frequency. The three horizontal dashed lines represent phase velocities of fast acoustic wave, entropy and vorticity waves, and slow acoustic wave, respectively. The excellent agreement of phase velocities at two different locations indicates that phase velocity is approximately a function of circular frequency only. The figure clearly shows that mode F originates from fast acoustic spectrum. As ω increases, phase velocity of mode F decreases. When mode F passes entropy and vorticity spectra near ω=0.1, there exists a jump of phase velocity, which is consistent with theoretical analysis of Fedorov and Khokhlov [21]. On the other hand, mode S originates from slow acoustic spectrum. The figure also shows that mode S synchronizes with mode F at the point of ω_s =0.11563 and a_s =0.93076.

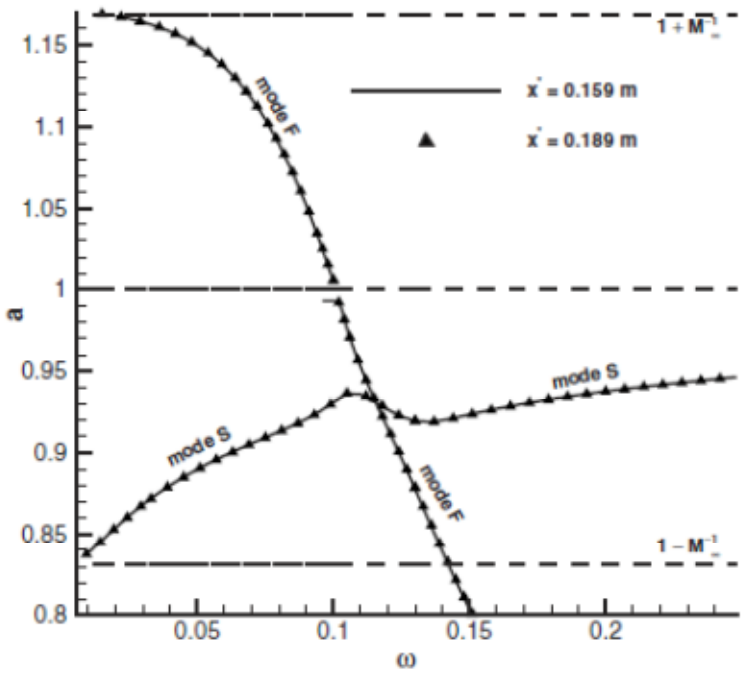

Figure 5. Distributions of phase velocities of boundary-layer waves at two different locations.

Although Figure 5 shows that the synchronization point has a constant value of circular frequency ω_s =0.11563, the location of the synchronization point in x coordinate, x_s, are different for different dimensionless frequencies F. The synchronization location in x coordinate for a given dimensionless frequency can be calculated using the following formula:

$$x_s = \frac{\left(\omega_s / F\right)^2}{\mathrm{Re}_\infty} \tag{21}$$

This equation indicates that the synchronization point moves upstream with dimensionless frequency increasing. Figure 6 shows growth rates of modes F and S at the same set of locations as a function of circular frequency. The horizontal dotted line stands for neutral waves α_i =0. In Figure 6, the growth rates of either mode S or mode F are approximately functions of circular frequency only. Mode S is always unstable, especially in the region from ω_I =0.00827 to ω_{II} =0.18465, whereas mode F is always stable. The parameters ω_I and ω_{II} are called branches I and II neutral points of mode S. The locations of branches I and II neutral points in x coordinate, which changes with different dimensionless frequencies, can be calculated by

$$x_I = \frac{\left(\omega_I / F\right)^2}{\mathrm{Re}_\infty}, x_{II} = \frac{\left(\omega_{II} / F\right)^2}{\mathrm{Re}_\infty} \tag{22}$$

Eq. (22) indicates that when F increases, the corresponding coordinates of branch points decrease. In other words, branches I and II neutral points move upstream when F increases. For wall blowing-suction disturbance at the frequency of $f = 100kHz$, the synchronization point and the branch II neutral points are located at 0.33184 m and 0.84622 m. More results on the LST analysis can be found in Wang and Zhong's paper [22].

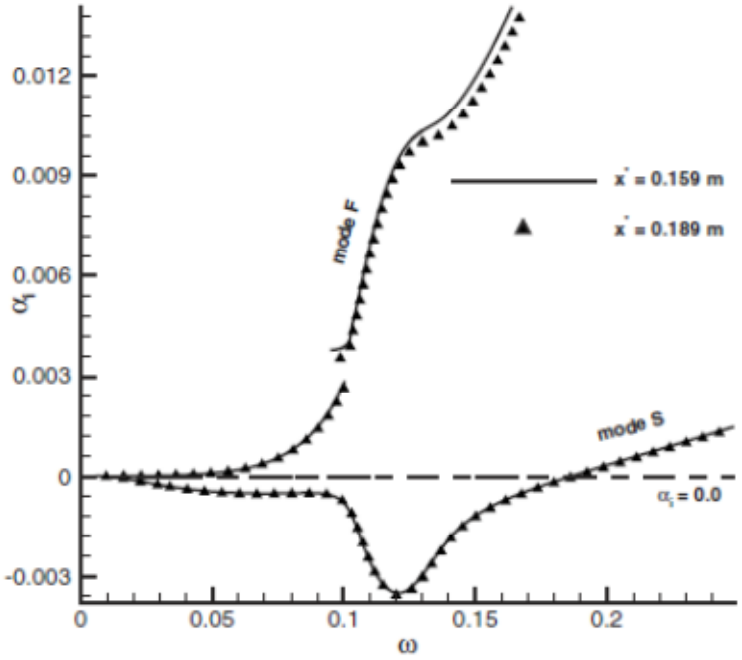

Figure 6. Distributions of growth rates of modes F and S at two different locations.

D. The role of roughness height and location on mode S and F

Using the LST analysis mentioned in the previous section, mode S and mode F for a Mach 5.92 flat-plate without roughness are numerically calculated and are imposed far upstream at x=0.069m for all test cases. Imposing the modes in the far upstream location can minimize the nonlinear effect due to roughness, thus ensures our LST result is still valid even for a flat plat with the existence of roughness. Figure 7 shows the wave mode profiles at

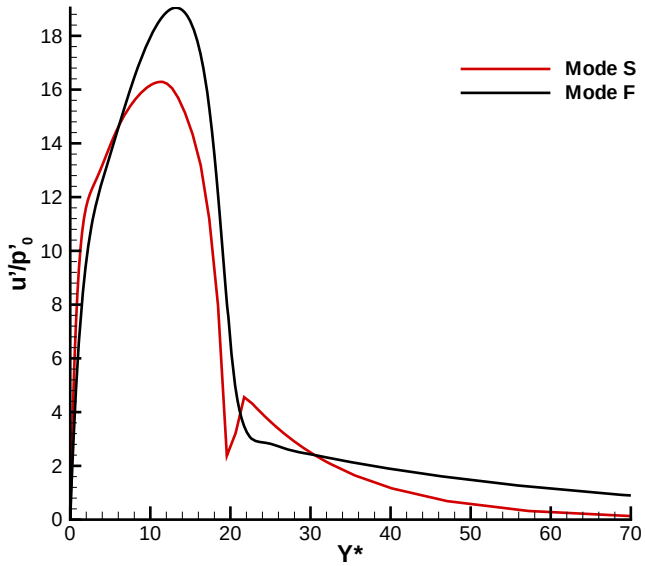

Figure 7. Mode S and Mode F profiles obtained by linear stability analysis at x=0.069m.

x=0.069m for both mode S and mode F obtained by linear stability analysis. The amplitude is normalized by the pressure disturbance on the wall, e.g. $u'(y) = \tilde{u}(y) / \tilde{p}(0)$. Figure 8 shows the amplitude of pressure disturbance due to mode S instability along the wall of flatplate without roughness. Since mode S is inherently unstable, the disturbance grows exponentially as expected. To validate our results, Wang and Zhong's result [23] is also included, it can been seen that they agree very well.

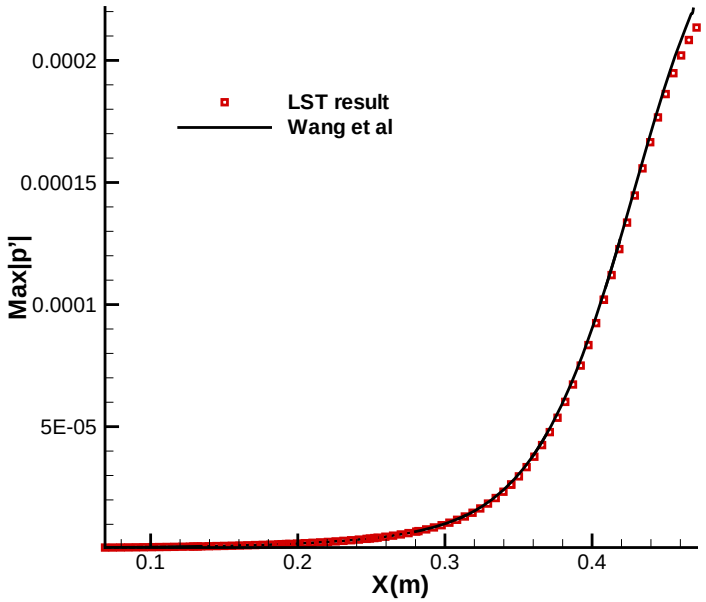

Figure 8.The amplitude of pressure disturbance due to Mode S instability for a flat plate without roughness.

In order to get a full picture of how roughness height and location affect modal growth. We have performed the following simulations,

Case 1: Roughness at far upstream of the synchronization point, x_r=0.1101m; Local boundary layer thickness;
$\delta = 1.448 \times 10^{-3}$ m; Roughness height 0.25δ, 0.375δ, 0.5δ, 0.625δ

Case 2: Roughness at upstream of the synchronization point, x_r=0.185m; Local boundary layer thickness $\delta = 1.61 \times 10^{-3}$ m; Roughness height 0.25δ, 0.375δ, 0.5δ, 0.625δ

Case 3: Roughness at the synchronization point, x_r=0.331m; Local boundary layer thickness $\delta = 2.82 \times 10^{-3}$ m; Roughness height 0.25δ, 0.375δ, 0.5δ, 0.625δ

Case 4: Roughness at downstream of the synchronization point, x_r=0.410m; Local boundary layer thickness $\delta = 3.42 \times 10^{-3}$ m; Roughness height 0.25δ, 0.375δ, 0.5δ, 0.625δ

As mentioned, the branch I neutral point or the first synchronization for 100kHz disturbance is located at x_s=0.331m. In the previous studies [16], it was found that the relative location of roughness and synchronization point can have a role in modal growth. Therefore, our roughness is placed according the relative location of synchronization point. In case 1, the roughness is located at far upstream of the synchronization point. We moved the roughness downstream in case 2. In case 3, the roughness is located at the synchronization point. Eventually, in case 4, we move the roughness downstream of synchronization point.

In addition to roughness location, the effect of roughness height is also of interest. We have varied the height of roughness from 25% to 62.5% local boundary layer thickness for each roughness location. Initially, roughness

height up to 75% of local boundary layer thickness is also tested. However, we found that we can never get a converged result for the meanflow. Therefore, for the scope of this paper, roughness is only up to 62.5%. Both mode S and mode F disturbance are imposed separately into the meanflow for all cases. 16 cases with roughness and one without roughness have been studied, and the results will be discussed next.

Figure 9 to Figure 12 show the mode S disturbance pressure contour for case 1 to case 4. In each case, roughness height has been varied from 25% to 62.5% the local boundary layer thickness. It can be seen that for all cases, the existence of roughness changes the disturbance significantly. For case 1 and case 2 (Figure 9 and Figure 10), the unsteady disturbance propagates downstream with its shape remain relatively unchanged. Once the disturbance hits the roughness, a secondary disturbance is created outside of boundary layer around the roughness. This secondary disturbance travels downstream with an angle similar to the bow shock. Nevertheless, this disturbance is not important in our study because it is outside the hypersonic boundary layer. In addition, it decays rapidly downstream that the magnitude is insignificantly compared with the disturbance trapped in the boundary layer.

In Figure 11 and Figure 12, the roughness is located at the synchronization point and downstream of it respectively. The secondary disturbance originated from the roughness can still be seen. On the other hand, for the trapped disturbance in the boundary layer that we are interested in, we can see that its magnitude increases far upstream and starts to damp as it approaches the roughness. This trend is different from what we observed in Figure 9 and Figure 10. In our most downstream and highest roughness case (Figure 12(d)), we can see that the disturbance has been damped very significantly.

Figure 13 to Figure 16 show the pressure disturbance along wall normal direction at one fixed x location. For each case, two locations are considered (upstream of roughness and downstream of roughness). In our most upstream case, roughness doesn't seem to have a strong effect on modal growth (Figure 13(a)). In case 2, roughness is able to amplify disturbance in the boundary layer in front of roughness (Figure 14(a)). Downstream of roughness, the secondary disturbance outside the boundary layer is very obvious (Figure 13(b) and Figure 14(b)). However, no obvious trend is observed for disturbance inside boundary layer. In case 3 where roughness is placed at synchronization point, it is shown in Figure 15(a) that tall roughness can damp disturbance in front of roughness. Moreover, the secondary disturbance is also present. Downstream of roughness (Figure 15(b)), disturbance is damped for all roughness height. The strength of secondary disturbance is weaker in this case. Figure 16 shows the plots for case 4. In this case, disturbance inside the boundary layer is greatly damped in front of roughness as well as downstream of it (Figure 16(a) and (b)).

To get a clearer picture of how the trapped disturbance in the boundary layer evolves with different roughness location and height, we have performed a FFT analysis on the flow field and plot the pressure amplitude on the wall at each roughness locations for each case as shown in Figure 17 to Figure 20.

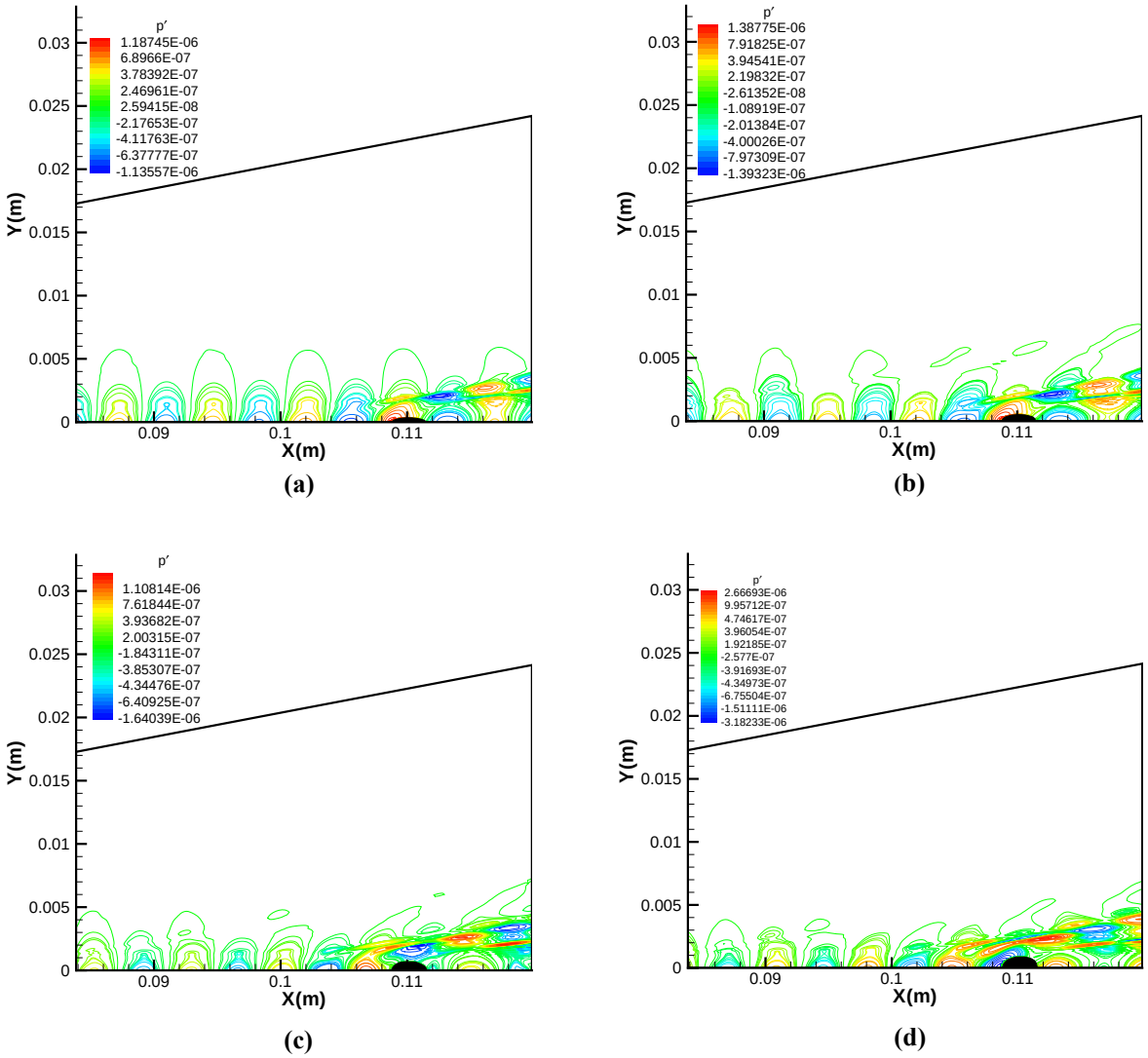

Figure 9. Mode S pressure disturbance contour for case 1, roughness at x_r=0.1101. (a) 0.25δ (b) 0.375δ (c) 0.5δ (d) 0.625δ

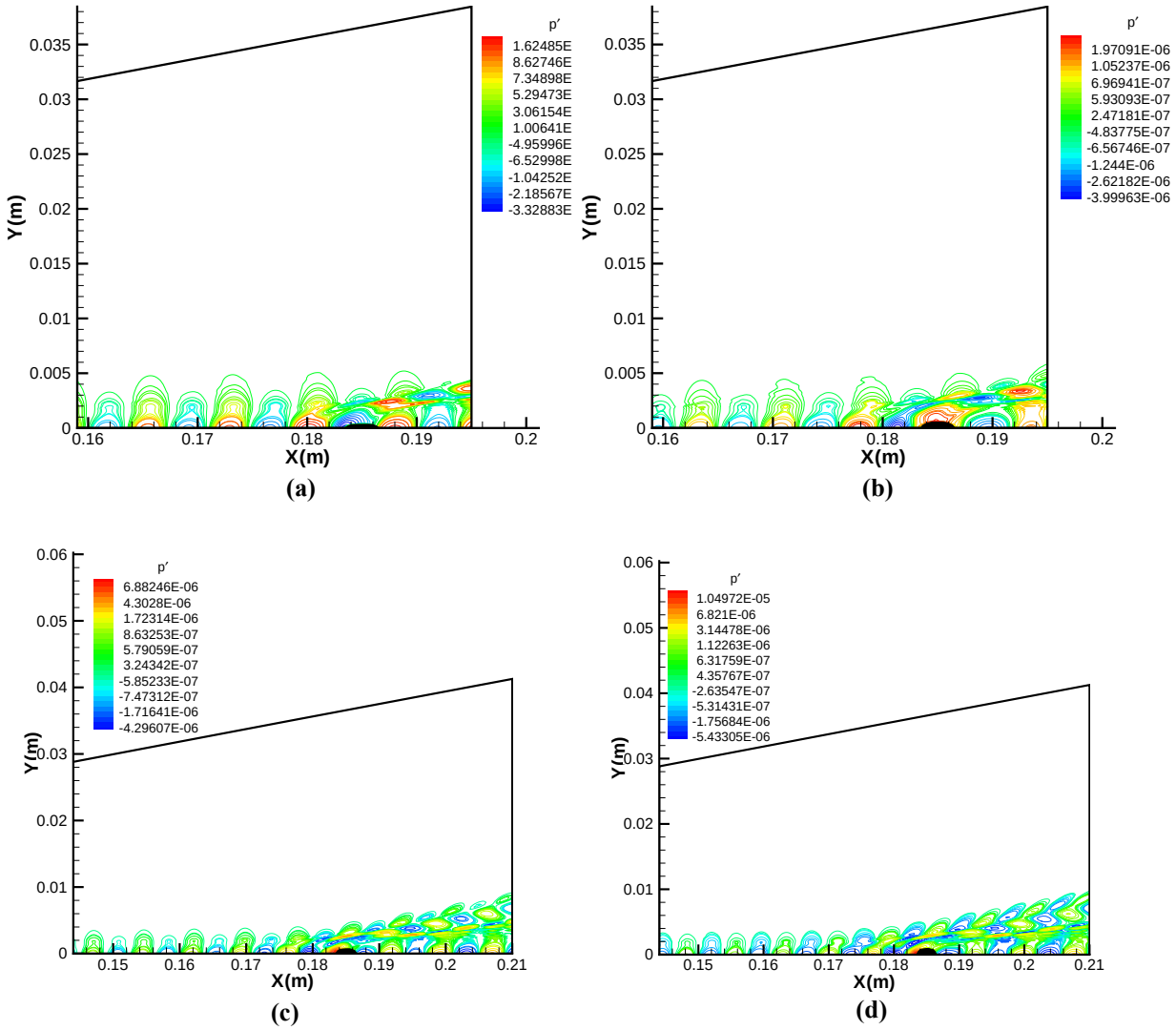

Figure 10. Mode S pressure disturbance contour for case 2, roughness at x_r=0.185. (a) 0.25δ (b) 0.375δ (c) 0.5δ (d) 0.625δ

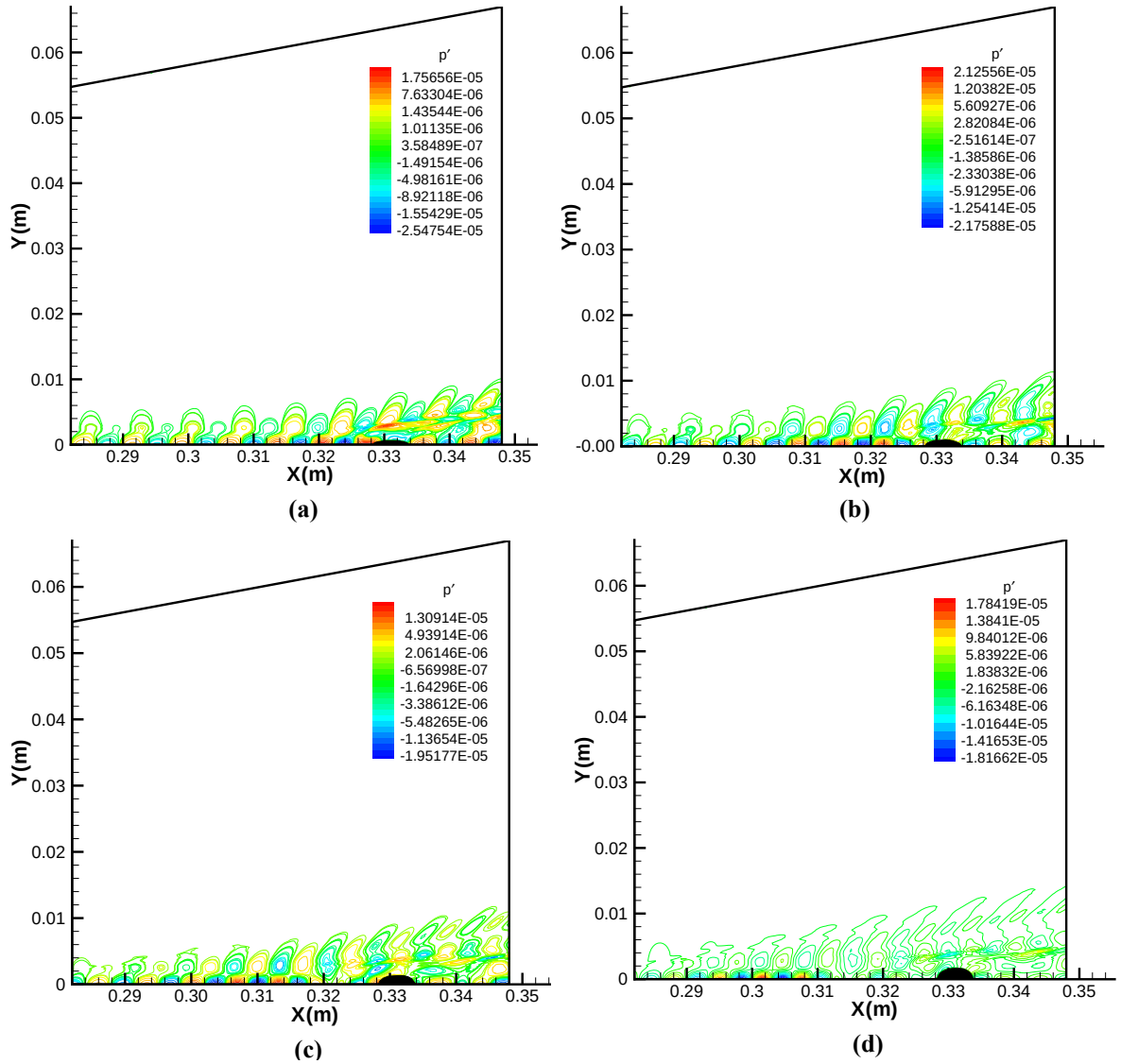

Figure 11. Mode S pressure disturbance contour for case 3, roughness at x_r=0.331. (a) 0.25δ (b) 0.375δ (c) 0.5δ (d) 0.625δ

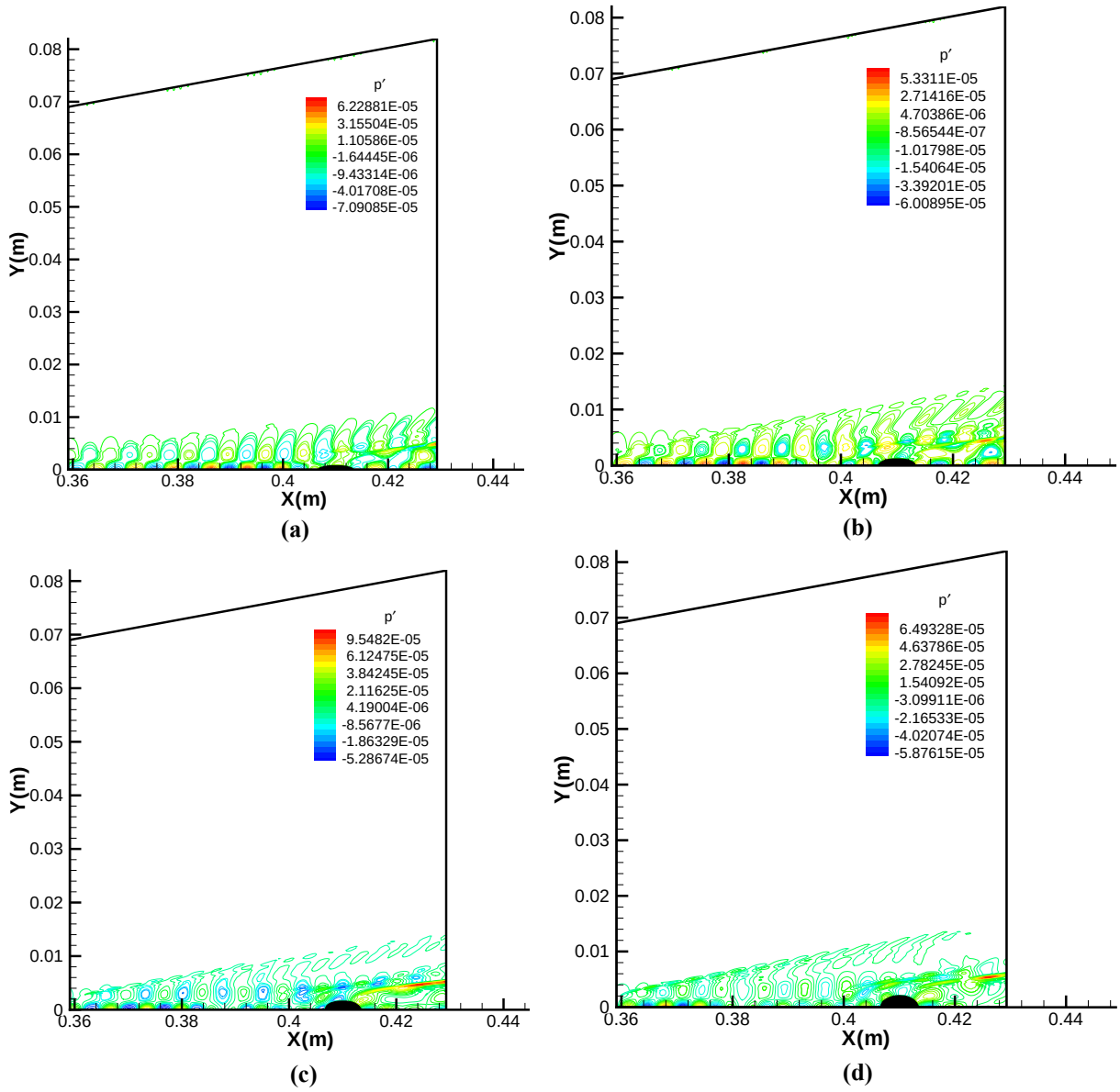

Figure 12. Mode S pressure disturbance contour for case 4, roughness at x_r=0.41. (a) 0.25δ (b) 0.375δ (c) 0.5δ (d) 0.625δ

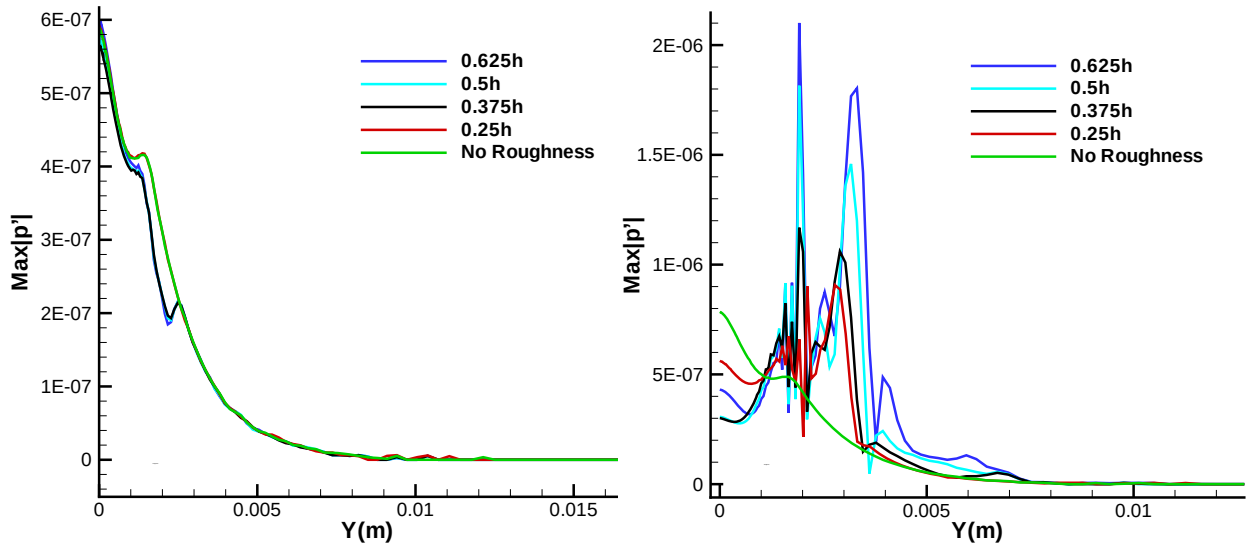

(a) **(b)**

Figure 13. Mode S pressure disturbance along wall normal direction y for case 1 x_r=0.1101m (a) upstream of roughness x=0.09m (b) downstream of roughness at 0.11685m

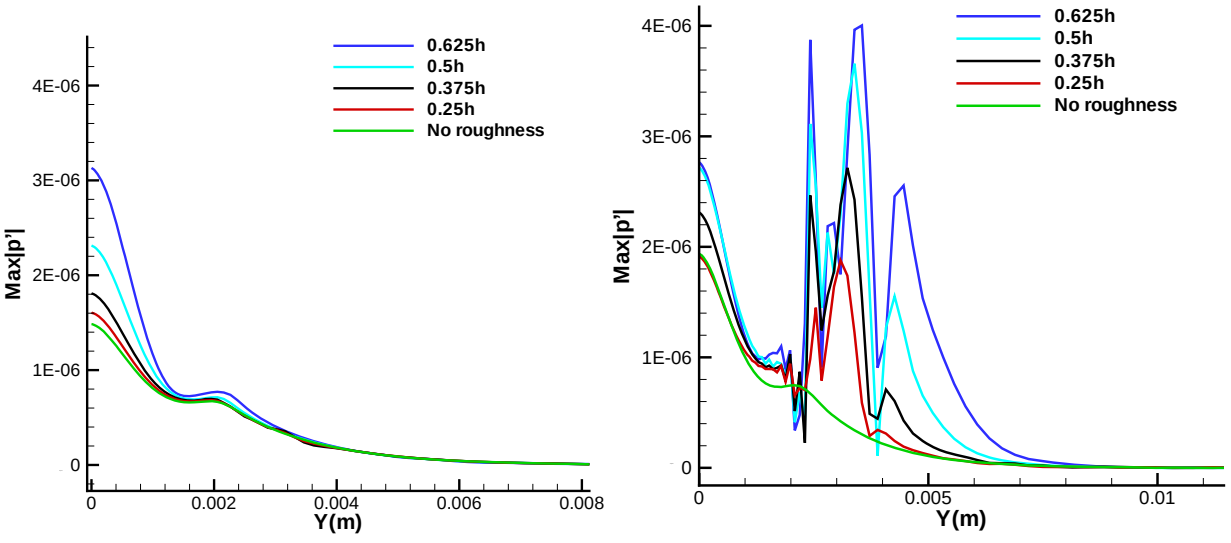

(a) **(b)**

Figure 14. Mode S pressure disturbance along wall normal direction y for case 2 x_r=0.185m (a) upstream of roughness x=0.17m (b) downstream of roughness at 0.192m

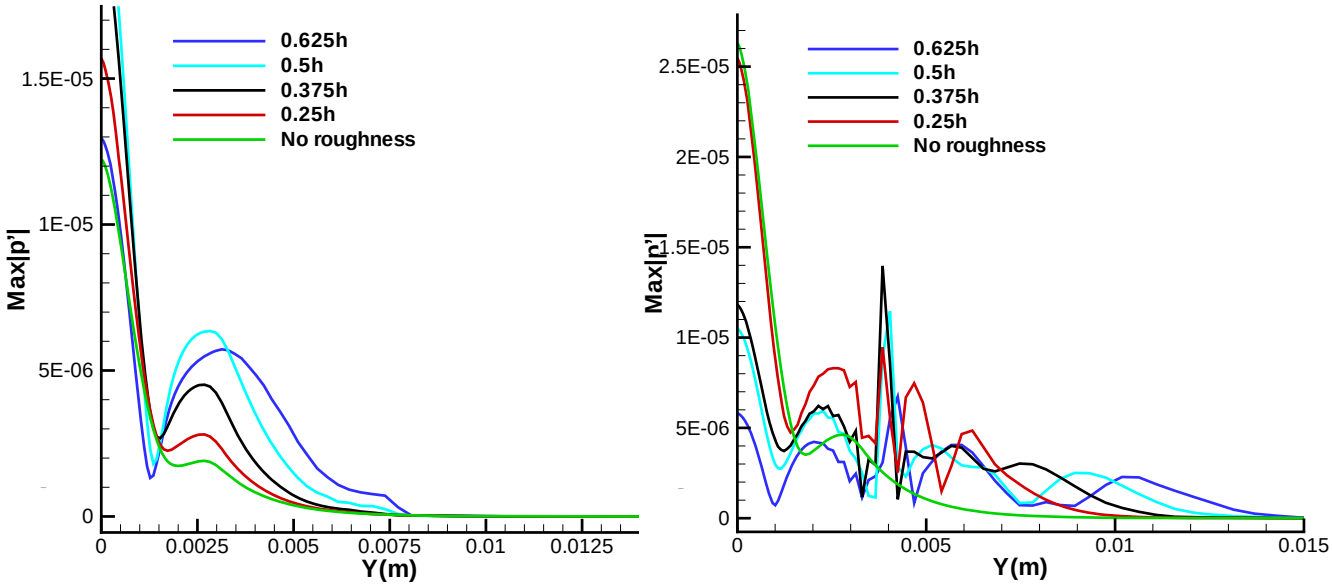

(a) (b)

Figure 15. Mode S pressure disturbance along wall normal direction y for case 3 x_r=0.331m (a) upstream of roughness x=0.310m (b) downstream of roughness at 0.345m

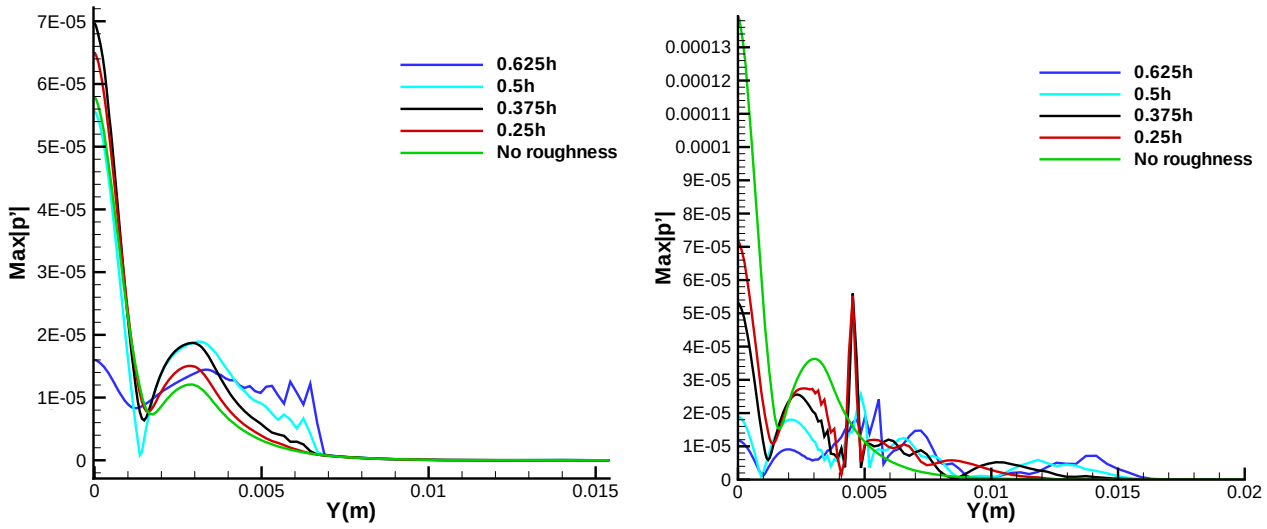

(a) (b)

Figure 16. Mode S pressure disturbance along wall normal direction y for case 4 x_r=0.410m (a) upstream of roughness x=0.380m (b) downstream of roughness at 0.4267m

Figure 17(a) and (b) show the growth of mode S pressure disturbance on the wall for case 1 and case 2 respectively. Since the algorithm of cut cell method doesn't solve for the grid points inside solid region, all disturbance drops back to zero inside the roughness element. That is responsible for the discontinuity in all our plots. The roughness of case 1 and case 2 are located upstream of synchronization point at x_r=0.1101m and x_r=0.185m respectively. In Figure 17(a), we can see that the disturbance for 0.375δ is damped a little bit in front of roughness before it starts to grow. The physical explanation is not known. But for all other cases, roughness upstream of synchronization point always amplifies disturbance upstream of roughness. The amplification rate depends strongly on the height of roughness. For example, in 0.25δ case, the maximum amplitude is just about 3 times than the case without roughness. In highest roughness case (0.625δ), the jump of amplitude can reach almost 13 times than without roughness. This amplification in the separation region upstream of roughness agrees with the result by Marxen et al [24].

Downstream of roughness, disturbance evolution has different trend depending on roughness location. In case 1, disturbance returns to the level as if there is no roughness, and no obvious trend is observed. However, in case 2 (Figure 17(b)), roughness height controls how the disturbance grows downstream of the roughness. It is found that disturbance is amplified for tall roughness (0.5δ and 0.625δ). For small roughness, the disturbance remains the same as the no roughness case. In general, roughness element tends to have more pronounced amplification effect in the vicinity upstream of roughness than downstream. Moreover, if roughness is placed too upstream of synchronization point, roughness tends to have small effect on modal growth.

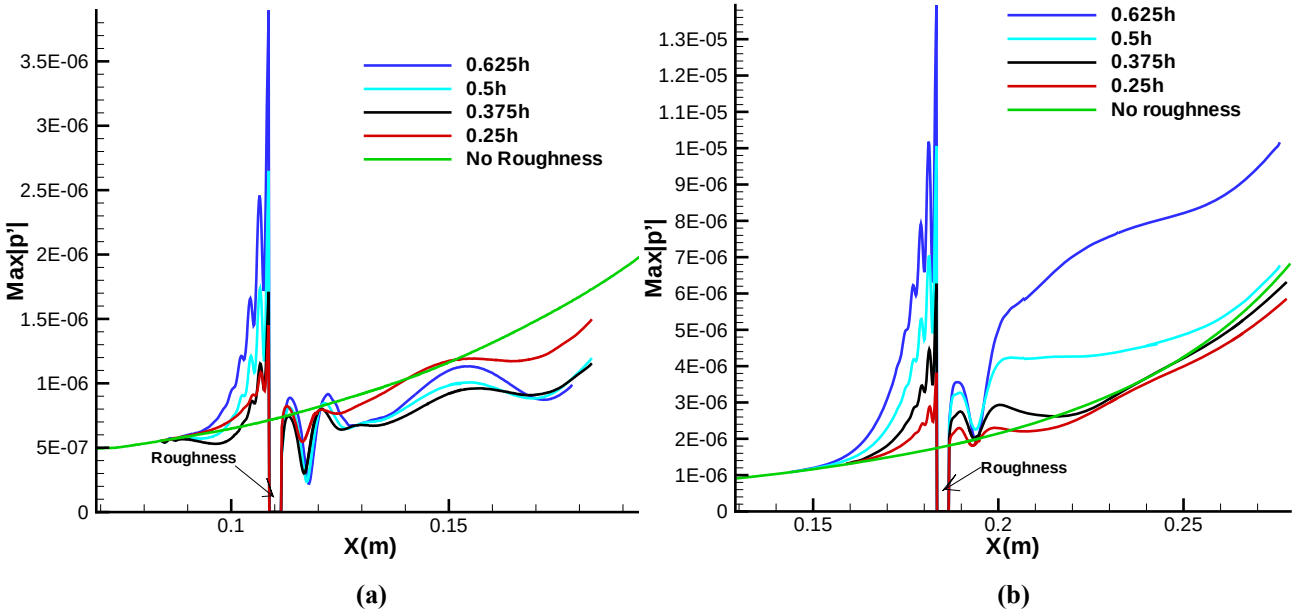

Figure 17. Mode S pressure disturbance on the wall with different roughness height. (a) case 1: roughness at 0.1101m. (b) case 2: roughness at 0.185m

As the roughness moves closer to the synchronization point in case 3 and case 4, we observe different trend for the growth of pressure disturbance. In Figure 18(a), the roughness sits exactly at the synchronization point. The disturbance for the smallest roughness (0.25δ) is still amplified and grows downstream as if there is no roughness. However, for taller roughness, disturbance only grows in far upstream region of the roughness. As disturbance travels closer to the roughness, it is suddenly damped. The location where disturbance starts to damp depends on roughness height. In 0.375δ roughness, damping starts at around x=0.317m. When roughness height increases to 0.5δ, the damping point moves to x=0.309m. Further increase in roughness height to 0.625δ moves the damping point even more upstream to x=0.303m. In the region between the point where disturbance starts to damp and the roughness, strong modulation of different modes is observed. Since modulation does not exist for the case without roughness, the modes which interact with the imposed mode must be generated by the roughness itself. Behind the

roughness, disturbance for small roughness (0.25δ) follows almost exactly the trend as without roughness. On the

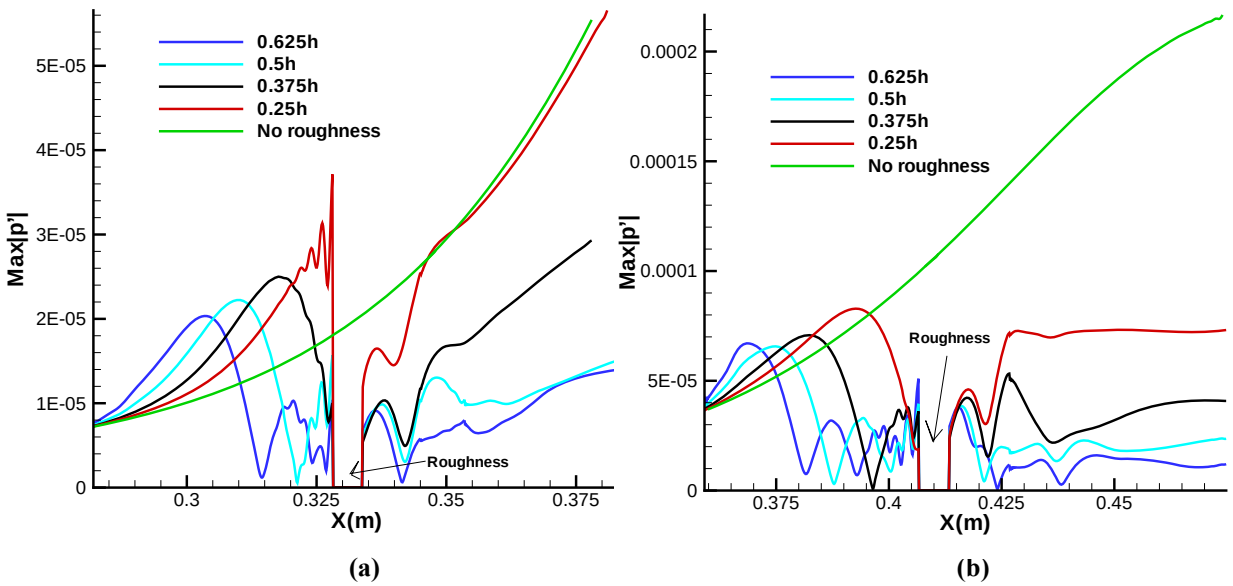

Figure 18. Mode S pressure disturbance on the wall with different roughness height. (a) case 3: roughness at 0.331m. (b) case 4: roughness at 0.41m

other hand, disturbance is still highly damped behind taller roughness. The taller the roughness, the weaker the pressure disturbance compared with the case without roughness. Tall roughness in this location acts as a disturbance damper instead of an amplifier like in case 1 and case 2, and the strength of damping depends on roughness height.

In the final test case, we moved the roughness even further downstream to x=0.41m, which is behind the synchronization point. Figure 18(b) shows how pressure disturbance reacts with different roughness height in this location. Similar to the case 3, disturbance is amplified in the far upstream region of roughness, but all damped when it gets close to the vicinity of roughness. One difference between this case and case 3 is all roughness height has damping effect even for our smallest roughness (0.25δ). In addition, the location where disturbance starts to be damped is more upstream of roughness than case 3. In the region behind roughness, disturbance for all cases stay at the same level and does not grow, which is significantly different from case 3. Judging from this result, we conclude that roughness in this location acts as a more effective disturbance damper than in case 3, which can potentially stabilize the flow.

Other than mode S disturbances, mode F is also found by LST and imposed into the same location at x=0.069m for the same 16 meanflows with roughness and one without roughness. The magnitude of mode F disturbance we imposed is about 100 times larger than mode S. The reason for this is mode F is inherently stable. If the magnitude is too small, numerical error would become very significant in the downstream region as the disturbance decays. In contrast, we know mode S is unstable and it grows exponentially, this kind of problem will not exist as long as the initial amplitude for mode S is larger than tolerance in numerical simulation. Figure 19(a) and (b) shows how the mode F pressure disturbance varies due to the existence of roughness for case 1 and case 2 respectively. For the case without roughness, we can see that the amplitude does not grow exponentially. This is due to the fact that mode F is stable. However, when the mode F disturbance travels further to a downstream region where is close to the synchronization point, it synchronizes with mode S in the meanflow and starts to grow exponentially. Both Figure 19(a) and (b) indicate this trend. The mode F disturbance grows exactly like Mode S in Figure 18 (a) and (b). After the synchronization point, our results show that mode S and F are indistinguishable.

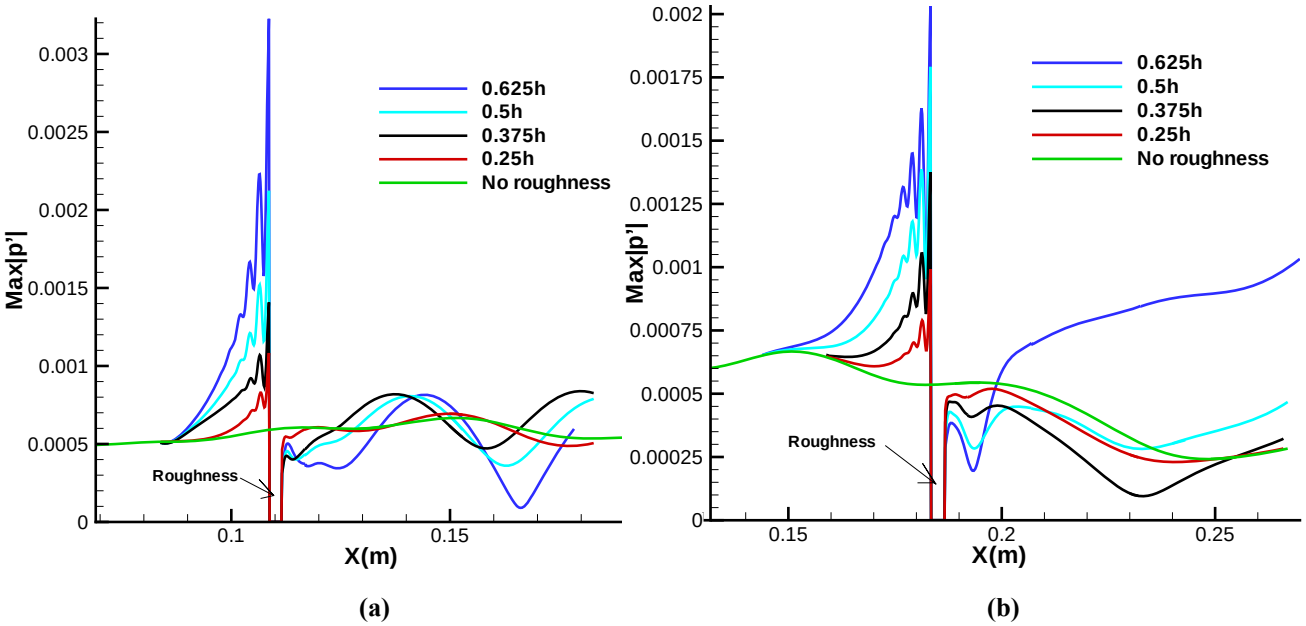

Figure 19. Mode F pressure disturbance on the wall with different roughness height. (a) case 1: roughness at 0.1101m. (b) case 2: roughness at 0.185m

The pressure amplitude of mode F for the most upstream case (x_r=0.1101) is shown in Figure 19 (a). Although different mode is imposed, the trend due to roughness is still very similar to the mode S result as shown in Figure 17(a). In other words, the disturbance is amplified upstream of roughness but returns to the level as no roughness downstream. The strength of amplification depends on the height of roughness. Moreover, in this case, we observed stronger modulation in the downstream vicinity of roughness than mode S. The tallest roughness results the strongest modulation downstream. Figure 19(b) shows the case which we place the roughness more downstream at x_r=0.185m. Upfront of roughness, the disturbance is amplified with strength according to roughness height. Nevertheless, in the downstream region, different roughness height exhibits different trends. Tall roughness (0.5δ and 0.625δ) seems to amplify disturbance effectively, while the disturbance for small roughness (0.375δ and 0.25 δ) looks very similar to the case without roughness. If we compare this result to the mode S result in the same location (Figure 17(b)), the two trends are very alike as if roughness does not 'feel' any difference between these two modes.

Figure 20 (a) and (b) show the cases which roughness locates at the synchronization point and downstream of it. As mentioned, when mode F disturbance gets close to the synchronization point, it becomes unstable similar to mode S. The exponential growth of disturbance we observed after synchronization point confirms this hypothesis. Subsequently, we expect the results for mode S and F in these two regions would not be very different. If we compare Figure 20 with Figure 18, it can be seen that the two trends are almost exactly the same. The only difference is the magnitude of disturbance.

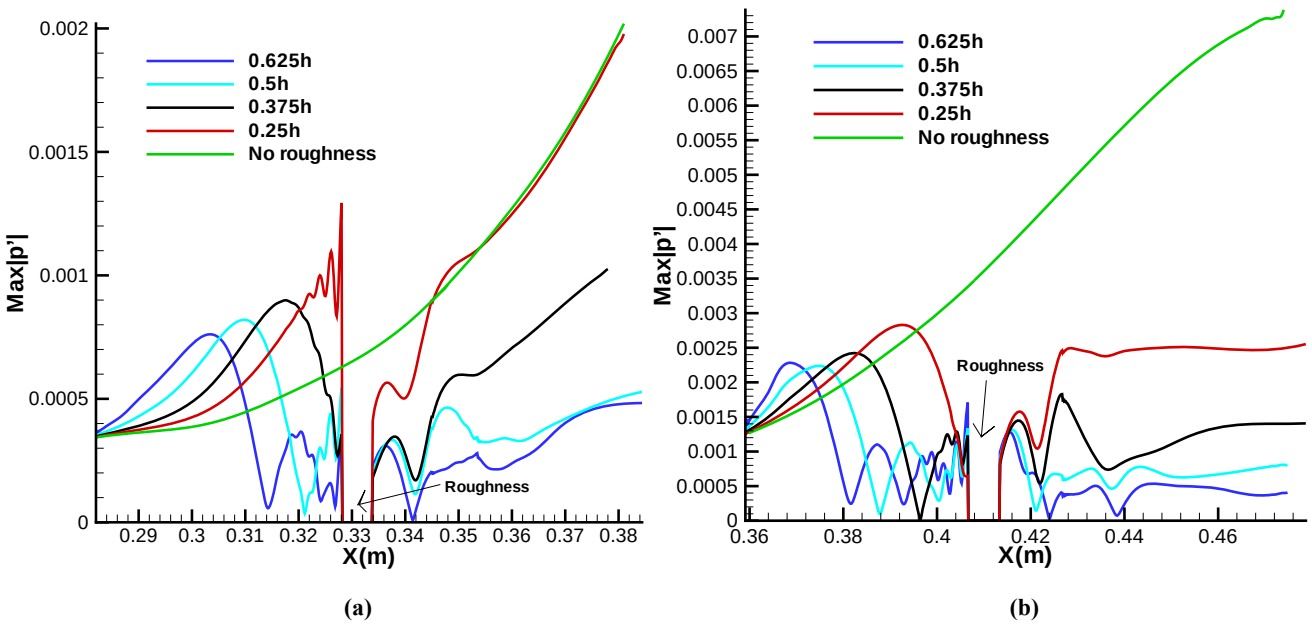

Figure 20. Mode F pressure disturbance on the wall with different roughness height. (a) case 3: roughness at 0.331m. (b) case 4: roughness at 0.41m

E. Discussion of results

In our investigation, it has been shown that roughness can either amplify or damp disturbance depending on the relative location between roughness and the synchronization point. Putting the roughness upstream of synchronization point amplifies disturbance and may probably trip the flow. In contrast, putting roughness at or downstream of synchronization point damps disturbance and may delay transition. We believe that our result can be a candidate to explain why roughness is able to stabilize a flow in some situation as some experiments have shown. For example, Holloway and Sterrett [25] concluded from their experiment in 1964 that "for a Mach number of 6.0, surface roughness that is less than the calculated boundary-layer velocity thickness at the roughness position can under certain conditions delay transition." However, they did not specify what condition led to the delay. Recently, Fujii [26] has investigated an efficient tripping method of a hypersonic boundary layer at Mach 7.1. To his surprise, he found that a wavy-wall roughness can suppress transition instead of expediting it. Although no physical explanation is given, the accurate repeatability results indicate that some unknown mechanisms must have presented. However, this delay mechanism is "still unknown, and remains so" [1]. Our results suggest that this mechanism can involve both the location of synchronization point for disturbance at particular frequency and roughness location. In particular, Holloway and Sterrett experiment shows that in high free stream unit Reynolds number, transition is delayed for small roughness. If one looks at our Eq.(23), it shows that higher free stream unit Reynolds number move synchronization upstream. We conjecture that in their high unit Reynolds number cases, the synchronization point had moved so upstream that it was in front of the roughness which, according to our results, could lead to suppression of disturbance. Although this is only a very brief observation and more studies are certainly needed to support this hypothesis, it provides us a light to explain roughness delay transition.

F. Future work

In our test cases, we have only considered disturbance with a fixed frequency at 100kHz. In order to get a better understanding of how roughness can affect disturbance with a range of frequency, we plan to impose a disturbance which consists of a board frequency range. One example of such disturbance is a Gaussian shape disturbance as shown in Figure 21(a). Figure 21 (b) shows a FFT analysis of such disturbance. It can be seen that it has a frequency range of 0Hz to 1 MHz. This range is sufficient to cover the unstable frequency domain. In our model, the disturbance will be imposed by a wall normal velocity on the wall of the same Mach 5.92 hypersonic flat plate. Although the disturbance is Gaussian shape in time, it is sinusoidal in space as shown in Figure 22. The sinusoidal shape can ensure we do not add any mass into the flow field. Figure 22 also shows that the center of our "hole" is

located far upstream at x=0.1m with a width about 3mm, which is an order of local boundary layer thickness. As a test case, we firstly use this model in a case without roughness. As shown in Figure 23, the disturbance is generated by a hole on the wall and the corresponding disturbance travels downstream. The period of the pulse is about 2.5 x 10^{-6} s. The hole is closed after one period, and no slip condition is applied. Figure 24 shows the FFT result for the disturbance on the wall at different x locations. The peaks at around 170 KHz indicate that the impulse disturbance has excited the unstable mode S inside the boundary layer. Since mode S is unstable, the peak grows as the sampling location gets downstream. We will apply this model to our roughness cases in the future. The goal of this study is to gain a deeper understanding of how roughness interacts with disturbance with different frequencies. In addition, study of roughness height and location will also be included. This study is motivated by Marxen et al [24] who have shown that "roughness can act as a disturbance amplifier with a limited bandwidth, which is capable of filtering a range of frequencies and strongly amplify only a selected range ." It will be interesting to compare their results with ours.

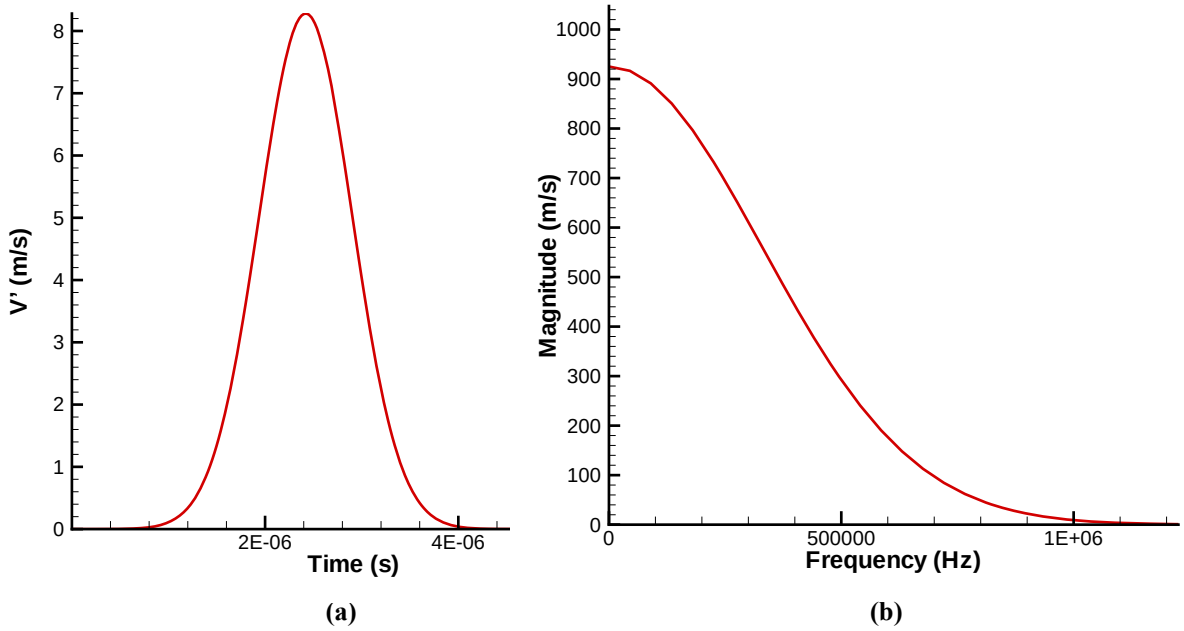

Figure 21. (a) Wall normal velocity Gaussian shape disturbance in time. (b) FFT result for the Gaussian sharp disturbance.

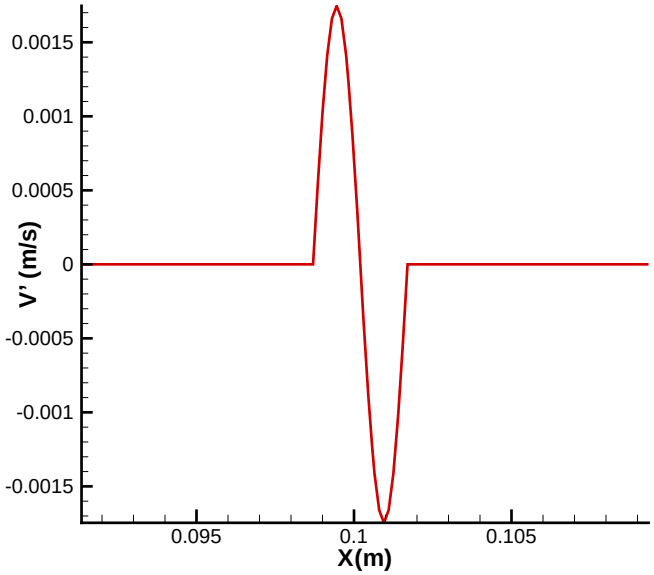

Figure 22. Snapshot of disturbance in space.

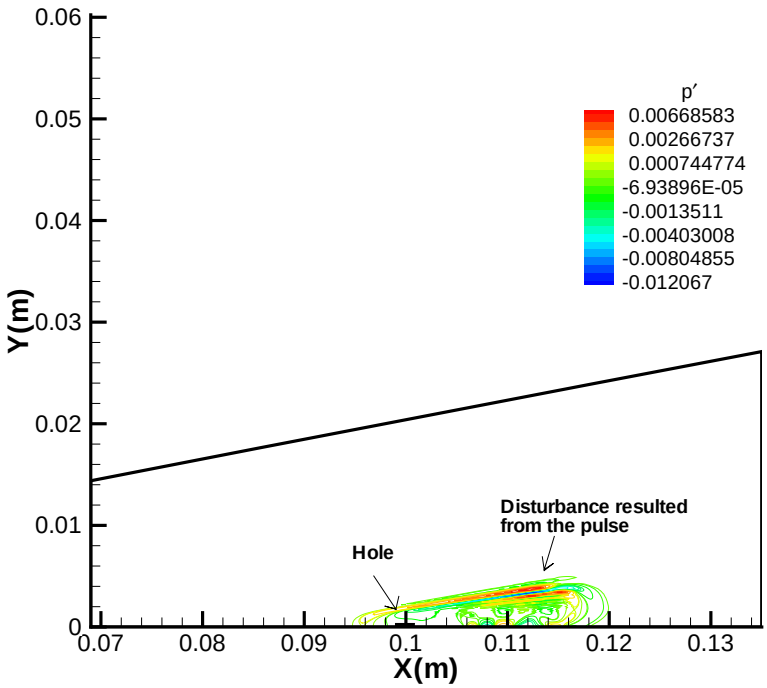

Figure 23. Pressure disturbance contour resulted from an Gaussian impulse for a case without roughness

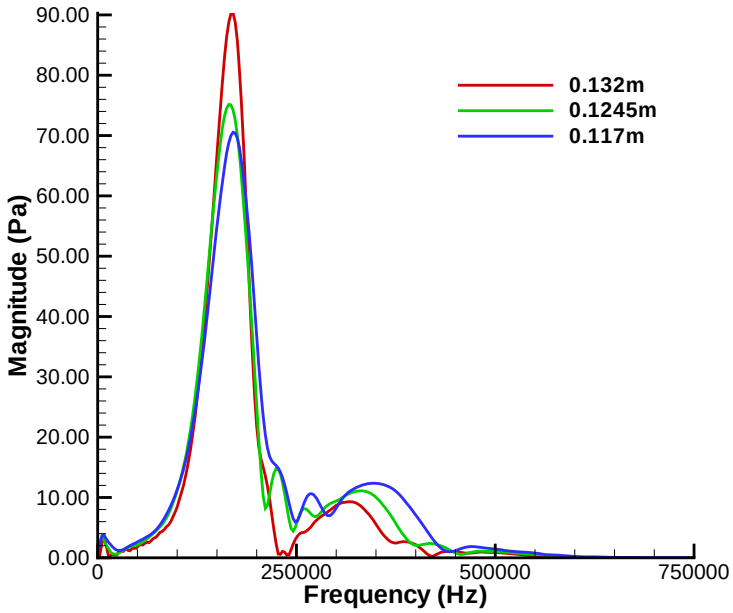

Figure 24. Frequency distribution obtained by FFT in different x-location

V.Summary

In this paper, we have further investigated the finite roughness effect on modal growth of a Mach 5.92 flat-plate boundary layer, mainly focusing on roughness height and roughness location. The steady base flow is firstly simulated by solving compressible Navier-Stokes equations. Stability characteristics of boundary-layer waves are analyzed by linear stability theory (LST). In stability simulations, two-dimensional disturbances corresponding to mode S or mode F at a frequency of 100 kHz are introduced near the leading edge. Four roughness locations relative to the synchronization point are considered. For each location, finite roughness with adjustable height is put downstream of the disturbances. Our results show that the location of roughness plays an important role on modal growth of two dimensional disturbances. If roughness locates very far upstream of synchronization point, disturbance is amplified in the upstream region of roughness, while the effect of roughness is not significant downstream. As roughness moves to a more downstream location, the overall amplification of two dimensional disturbance is very strong for tall roughness. This strong amplification may lead to early transition of hypersonic boundary layer. Our result also shows that roughness is capable of damping disturbance. When roughness is placed at synchronization point, we observed roughness acts as a disturbance damper. The tallest roughness results the strongest strength of damping. This damping effect gets more pronounced as roughness is placed more downstream of synchronization point. We believe that this result may explain some previous experiments in which roughness has delayed transition instead of expediting it. Additionally, we find that the difference between mode S and mode F on roughness is very minimal. Our future plan involves implementing a disturbance with a board range of frequency. The comparison with existing numerical results available will be interesting.

Acknowledgments

This work was sponsored by the Air Force Office of Scientific Research, USAF, under AFOSR Grant #FA9550-07-1-0414, monitored by Dr. John Schmisseur. This work was also sponsored by the AFOSR/NASA National Center for Hypersonic Research in Laminar-Turbulent Transition. The views and conclusions contained herein are those of the author and should not be interpreted as necessarily representing the official policies or endorsements either expressed or implied, of the Air Force Office of Scientific Research or the U.S. Government.

References

1. Schneider, S.P., *Summary of hypersonic boundary-layer transition experiments on blunt bodies with roughness, J. Spacecraft and Rockets.* Journal of Spacecraft and Rockets, 2008. **45**: p. 1090-1112.
2. Board, D.S., *Final report of the second defense science board task force on the national aero-space plane (NASP)*, 1992. p. 94-00052.
3. Anderson, J.D., *Hypersonic and high temperature gas dynamics*. 2000: AIAA.
4. Berry, S., Horvath, T., *Discrete roughness transition for hypersonic flight vehicles*, in *45th AIAA Aerospace Sciences Meeting and Exhibit*2007: Reno, Nevada.
5. Saric, W.S., Reed, H. L., and Kerschen, E. J., *Boundary-Layer Receptivity to Freestream Disturbances.* Annual Review of Fluid Mechanics, 2002. **34**: p. 291-319.
6. Mack, L.M., *Boundary layer linear stability theory*, in *AGARD Report*1984. p. 1-81.
7. Maslov, A.A., Shiplyuk, A. N., Sidorenko, A., and Arnal, D., *Leading-edge Receptivity of a Hypersonic Boundary Layer on a Flat Plate.* Journal of Fluid Mechanics, 2001. **426**: p. 73-94.
8. Maslov, A.A., Mironov, S. G., Shiplyuuk, A. A., Sidorenko, A. A., Buntin, D. A., and Aniskin, V. M., *Hypersonic Flow Stability Experiments.* 2002. **AIAA 2002-0153**.
9. Demetriades, A., *Hypersonic Viscous Flow Over A Slander Cone. Part III: Laminar Instability and Transition.* AIAA paper 74-535, 1974.
10. Demetriades, A., *Laminar Boundary Layer Stability Measurements at Mach 7 Including Wall Temperature Effects.* AFOSR-TR-77-1311, 1977.
11. Malik, M.R., Lin, R. S., and Sengupta, R., *Computation of Hypersonic Boundary-Layer Response to External Disturbances.* AIAA paper 1999-0411, 1999.
12. Ma, Y., and Zhong, X., *Receptivity to Freestream Disturbances of Mach 8 Flow over A Sharp Wedge.* AIAA paper 2003-0788, 2003.
13. Wang, X., Zhong, X., and Ma, Y., *Response of a hypersonic boundary layer to wall blowing - suction.* AIAA Journal, 2011. **In press**.
14. Balakumar, P. *Transition In a Supersonic Boundary-Layer Due To Roughness Aand Acoustic Disturbances*. in *AIAA*. 2003.
15. Marxen, O., Iaccarino, G., *Numerical simulation of the effect of a roughness element on high-speed boundary-layer instability*, in *38th Fluid Dynamics Conference and Exhibit*2008: Seattle, Washington.
16. Duan, L., Wang, X., and Zhong, X., *A High-Order Cut-Cell Method for Numerical Simulation of Hypersonic-Boundary Transition with Arbitrary Surface Roughness.* AIAA paper 2009-1337, 2009.
17. Duan, L., Wang, X., and Zhong, X. , *A high-order cut-cell method for numerical simulation of hypersonic boundary-layer instability with surface roughness.* Journal of Computational Physics, 2010. **229**(19): p. 7207-7237.
18. Whitehead, A.H., *Flow field and drag characteristics of several boundary-layer tripping elements in hypersonic flow.* Techinical paper, NASA, 1969. **5454**.
19. Lee, C.H., Chu, Y. H., *A New Type of TVD Schemes for Computations of High Speed Flows*, in *AIAA*1993.
20. Malik, M.R., *Numerical methods for hypersonic boundary layer stability.* Journal of Compuational Physics, 1990. **86**(2): p. 376 - 413.
21. Fedorov, A.V., and Khokhlov, A. P., *Prehistory of Instability in a Hypersonic Boundary Layer.* Theoretical and Computational Fluid Dynamics, 2001. **14**: p. 359-375.
22. Wang, X., and Zhong, X., *Effect of wall perturbations on the receptivity of a hypersonic boundary layer.* Physics of fluids, 2009. **21** (044101).
23. Wang, X., and Zhong, X., *Effect of porous coating on boundary-layer instability.* AIAA Paper 2010-1243, 2010.
24. Marxen, O., Iaccarino, G. and Shaqfeh,E.S.G., *Disturbance evolution in a Mach 4.8 boundary layer with two-dimensional roughness-induced separation and shock.* Journal of Fluid Mechanics, 2010. **648**: p. 435-469.
25. Holloway, P.F.a.S., J.R., *Effect of controlled surface roughness on boundary-layer transition and heat transfer at Mach numers of 4.8 and 6.0*, 1964, NASA.
26. Fujii, K., *An Experiment of Two Dimensional Roughness Effect on Hypersonic Boundary-Layer Transition*, in *43rd AIAA Aerospace Sciences Meeting and Exhibit*2005: Reno, Nevada.